

Beginner's Guide to Interpreting Defect and Defect Level Diagrams

Prashun Gorai^{*}*Rensselaer Polytechnic Institute, Troy, New York 12180, USA*

(Received 20 June 2025; published 22 August 2025)

Point defects are ubiquitous in materials and play a critical role in determining their electrical, optical, ion-transport, and other properties, making them key to the performance of materials in energy applications. First-principles defect calculations, particularly those based on density functional theory, are powerful tools for predicting defect energetics and associated electronic properties. However, the results are often communicated through defect formation energy diagrams and defect level diagrams, which can be challenging to interpret for researchers who do not specialize in defect physics. This Tutorial provides a practical accessible guide for understanding and interpreting these diagrams, with a focus on materials with a band gap—semiconductors and insulators. Aimed at experimentalists and computationalists new to defect analysis, the Tutorial explains how to extract key physical insights from defect diagrams, such as defect and carrier concentrations, dopability, midgap states, and charge localization. By demystifying the language and visuals of defect calculations, this guide seeks to bridge the gap between theory and experiments, enabling broader use of defect data in the rational design of functional materials for energy applications and beyond.

DOI: [10.1103/jtyg-xry3](https://doi.org/10.1103/jtyg-xry3)

CONTENTS

I. INTRODUCTION	1
II. WHAT ARE DEFECT AND DEFECT LEVEL DIAGRAM?	2
III. HOW ARE DEFECT DIAGRAMS PLOTTED?	3
IV. WHAT DOES THE CHARGE STATE OF A DEFECT SIGNIFY?	3
V. WHAT ARE CHARGE-TRANSITION OR DEFECT LEVELS?	3
VI. WHAT ARE SHALLOW AND DEEP DEFECTS?	4
VII. WHAT IS THE EFFECT OF ELEMENTAL CHEMICAL POTENTIALS?	6
VIII. HOW ARE DEFECT AND ELECTRONIC CARRIER CONCENTRATIONS CALCULATED?	6
IX. HOW IS THE EQUILIBRIUM FERMI ENERGY ESTIMATED? WHAT INSIGHTS CAN BE GAINED?	7

X. CAN A MATERIAL BE DOPED <i>n</i> - or <i>p</i> -TYPE? WHAT DETERMINES DOPABILITY?	7
A. Scenario 1 (<i>p</i> -type dopable)	8
B. Scenario 2 (<i>n</i> -type dopable)	8
C. Scenario 3 (<i>n</i> - and <i>p</i> -type dopable)	9
D. Scenario 4 (not <i>n</i> - or <i>p</i> -type dopable)	9
XI. PRACTICAL EXAMPLES FROM ENERGY RESEARCH	10
A. Photovoltaics—Defects in halide perovskites	10
B. Thermoelectrics—Dopability of Mg ₃ Sb ₂	10
C. Solid-state batteries—Diffusion mechanism and aliovalent doping of Na ₃ SbS ₄	11
D. Power electronics—Dopability and doping of β-Ga ₂ O ₃	12
XII. CONCLUDING REMARKS	13
ACKNOWLEDGMENTS	13
DATA AVAILABILITY	13
REFERENCES	13

I. INTRODUCTION

Point defects such as vacancies, interstitials, and anti-sites are natively present in all crystalline and amorphous solids and can strongly influence material properties. In semiconductors and insulators, which possess a band gap between the valence and conduction bands, these defects play a decisive role in governing electronic and optical [1–3], ion transport [4,5], and mechanical behavior [6], among other properties. From an energy-materials

^{*}Contact author: goraip@rpi.edu

Published by the American Physical Society under the terms of the [Creative Commons Attribution 4.0 International](https://creativecommons.org/licenses/by/4.0/) license. Further distribution of this work must maintain attribution to the author(s) and the published article's title, journal citation, and DOI.

perspective, point defects are central to many functionalities: they mediate carrier recombination in photovoltaic absorbers and light emitters, affect ionic conductivity in solid ion conductors, and influence charge transport in small bandgap materials for thermoelectrics and wide bandgap materials for power electronics.

First-principles defect calculations, especially those based on density functional theory (DFT), are now widely used to predict the formation energetics of point defects and associated electronic properties [7–11]. These calculations are often summarized through defect formation energy diagrams (in short, “defect diagrams”) and charge transition level diagrams (also, “defect level diagrams”). In the literature, the term “transition level diagram” is often used to refer to what is termed a “defect diagram” in this Tutorial—namely, a plot showing the formation energies of different charge states of a defect as a function of the Fermi energy. While these visualizations are powerful tools, they can be difficult to interpret for those unfamiliar with the underlying formalism. Yet, a basic understanding of these diagrams can yield rich physical insights. For example, one can estimate the equilibrium defect and carrier concentrations, evaluate doping feasibility (*p*-type, *n*-type, or ambipolar), identify midgap traps that limit device efficiency, or understand the nature of localized electronic states such as small polarons—all of which are essential for rational design and optimization of materials for energy applications.

This *Beginner’s Guide to Interpreting Defect and Defect Level Diagrams* Tutorial is aimed at helping a broad research community, including experimentalists and computationalists new to defect studies, make sense of the results reported in defect-focused papers. Our goal is not to teach how to perform defect calculations but to empower readers to confidently interpret defect diagrams and energy level diagrams, connect theoretical predictions to experimental observables, and apply these insights to materials discovery and design in energy-relevant contexts such as photovoltaics, batteries, fuel cells, thermoelectrics, power electronics, etc. Through intuitive explanations and practical examples, I hope to make defect diagrams accessible and useful to a wider audience in the energy-materials field and beyond.

II. WHAT ARE DEFECT AND DEFECT LEVEL DIAGRAM?

The formation energies of point defects are calculated using the supercell approach, as detailed in previous studies [7,9,11], with an excellent practical quick-start guide provided in Ref. [12]. Software packages have been developed to automate parts of these calculations, especially the calculation setup and post processing [13–16]. The results of these calculations are commonly visualized using defect formation energy diagrams (or “defect diagrams”)

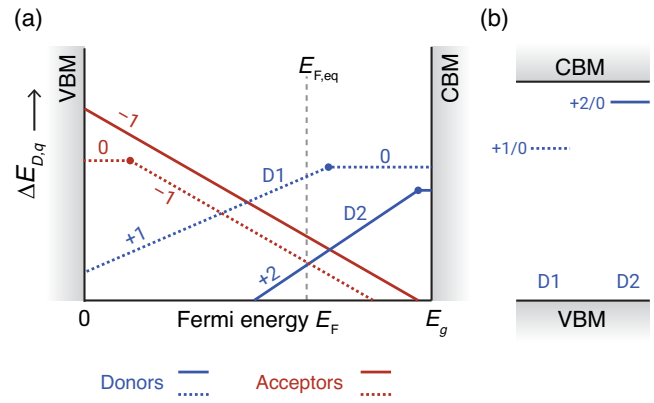


FIG. 1. (a) A schematic defect diagram of the defect formation energy ($\Delta E_{D,q}$) plotted against the Fermi energy (E_F) for multiple defects. (b) A corresponding defect level diagram showing the charge-transition levels of defects D1 and D2 in (a).

and defect level diagrams, both of which are discussed below. These diagrams serve as valuable tools for both the qualitative evaluation of defect and doping behavior (e.g., dopability) and the quantitative estimation of defect concentrations and electronic charge carrier (electron and hole) populations. The focus of this discussion is on semiconductors and insulators—materials characterized by a finite band gap. In a defect diagram, the formation energy of each defect ($\Delta E_{D,q}$) is plotted as a function of the Fermi energy (E_F), typically referenced to the valence band maximum (VBM), such that $E_{F,VBM} = 0$. Here, D is the defect type and q is the charge state of the defect. A schematic example is shown in Fig. 1(a), where E_g denotes the band gap.

Note: The defect diagrams are plotted at a chosen elemental chemical-potential (μ_i) condition. Here, μ_i for every element i should be within the range in which the material is thermodynamically stable against decomposition into competing phases. These ranges are determined from a grand potential phase diagram.

The defect level diagram, also referred to as the charge transition level (CTL) or energy level diagram, is a visual representation of the electronic states introduced by defects. These diagrams are typically plotted along the energy axis spanning from the VBM to the conduction band minimum (CBM) and show where defect-related states occur within the band gap. Defect level diagrams [e.g., Fig. 1(b)] are constructed directly from defect formation energy diagrams. Specifically, they plot the energy corresponding to changes in the slope of the defect lines, i.e., the charge transition levels, which are discussed in more detail later. Each transition is labeled according to

the initial and final charge states, as illustrated in Fig. 1(b) for example defects D1 and D2. These diagrams are typically plotted with energy on the vertical axis, providing an intuitive view of where defect levels lie relative to the band edges.

Note: While defect level diagrams offer insight into the position of defect states, they do not convey information about defect formation energies. As such, they can be misleading when used in isolation, particularly when assessing the practical impact of a defect on material properties. For example, a defect that introduces a deep midgap level may appear important in a defect level diagram, but if its formation energy is high, its equilibrium concentration will be low, and it may have negligible effect on the electronic properties. Thus, defect level diagrams should always be interpreted alongside formation energy data, especially when evaluating the quantitative influence of defects on materials properties.

III. HOW ARE DEFECT DIAGRAMS PLOTTED?

Each set of connected lines in Fig. 1(a) (solid red, dotted red, solid blue, and dotted blue) represents a defect D , which could be, e.g., a cation vacancy or a substitutional dopant. The slope of the line is the charge state q of the defect D . $\Delta E_{D,q}$ linearly depends on E_F and is given by

$$\Delta E_{D,q} = E_{D,q} - E_H + \sum_i n_i \mu_i + E_{\text{corr}} + qE_F. \quad (1)$$

For a defect D , conventionally only the charge state q with the lowest $\Delta E_{D,q}$ at a given E_F is plotted. This method of plotting the data is motivated by two reasons: (1) to improve readability of the defect diagrams, and (2) the charge state q with lowest $\Delta E_{D,q}$ has the highest concentration at that E_F . This is illustrated schematically for a defect in Fig. 2.

Note: Even though only the charge state q with the lowest $\Delta E_{D,q}$ is plotted at a given E_F , in reality, a nonzero Boltzmann population of other charge states exists.

IV. WHAT DOES THE CHARGE STATE OF A DEFECT SIGNIFY?

Charged defects can generate electronic carriers (electrons or holes), whereas neutral defects, such as those arising from isoelectronic doping or alloying, do not contribute free carriers. In a defect diagram, positively charged

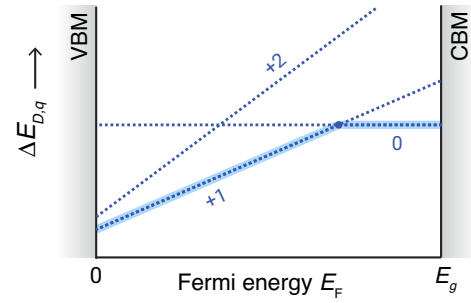


FIG. 2. For a defect, charge states with the lowest $\Delta E_{D,q}$ at a given E_F are plotted. Only charge states +1 and 0 will be typically plotted, leaving out the +2 charge state.

defects exhibit a positive slope and are classified as donor-like (Fig. 3). These defects ionize by donating one or more electrons, thereby becoming positively charged. Donor-like defects generally promote n -type conductivity by increasing the electron concentration. Conversely, negatively charged defects have a negative slope in the defect diagram and are considered acceptor-like. These defects accept electrons, effectively generating holes and tending to make the material p -type.

It is important to note, however, that whether a material is ultimately doped n -type or p -type depends on several additional factors, which will be discussed after introducing a few more key concepts.

V. WHAT ARE CHARGE-TRANSITION OR DEFECT LEVELS?

The charge transition level (CTL) of a defect, denoted as q/q' , is defined as the Fermi energy at which the formation energies of two charge states, q and q' , are equal. In a defect diagram, CTLs appear as points at which the slope of a defect line changes, indicating a transition between different charge states. A single defect may exhibit multiple CTLs within the band gap or none at all. As illustrated

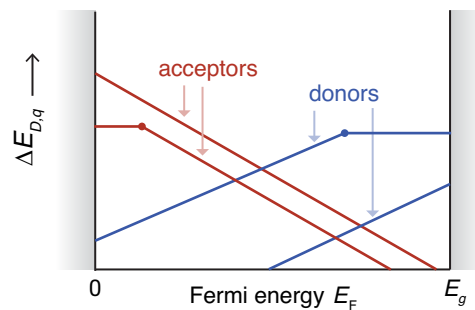


FIG. 3. Positively charged defects (positive slope) are donor defects. Similarly, acceptor defects are negatively charged and, therefore, the defect lines exhibit negative slope.

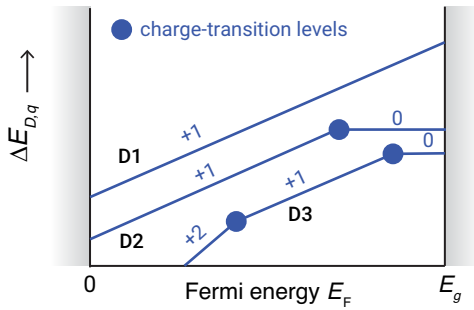


FIG. 4. The charge transition levels of deep and shallow defects.

in Fig. 4, defect D1 has no CTLs, D2 has one CTL, and D3 exhibits multiple CTLs within the band gap.

Physically, these CTLs correspond to the energetic positions of defect-induced electronic states within the band gap. Such states can trap charge carriers and strongly influence carrier dynamics, recombination processes, and transport properties. While a detailed discussion of these effects lies beyond the scope of this Tutorial, it is important at this stage simply to recognize the presence and significance of these defect states. CTLs provide a link between atomistic defect models and experimentally observable phenomena. Several experimental techniques can probe these defect levels:

- (a) *Deep-level transient spectroscopy* (DLTS) is a powerful tool for detection and identification of deep defect levels (also, trap states) in semiconductors [17]. DLTS measures the activation energy of deep defect levels within the band gap by monitoring transient capacitance signals. The energy levels observed in DLTS often correspond closely to CTLs predicted by first-principles defect calculations.
- (b) *Photoluminescence* (PL) spectroscopy provides signatures of defects by analyzing the light emitted after excitation. The light emitted during the transition of electrons between valence and conduction bands and defect levels within the band gap, including between defect levels, has unique spectral characteristics. These characteristics, including the wavelength, intensity, and linewidth of the emitted light, can be used to identify the types and concentrations of defects [18–20]. For example, the radiative transition of an excited electron from the conduction band to an unoccupied defect level may produce a photon the energy of which corresponds to the energetic difference between the CBM and the defect level. By analyzing the photon energy, one can infer how far (energetically) the defect level is from the CBM.
- (c) *Electron paramagnetic resonance* (EPR) spectroscopy provides signatures of defects by detecting

the magnetic moments of unpaired electrons within those defects. The presence of defects with unpaired electrons leads to distinct spectral features, such as different g values and signal intensities, which can be used to identify the types and concentrations of defects [21–23]. One must note that not all defects feature unpaired electrons and, hence, cannot be observed with EPR spectroscopy.

- (d) *Thermoluminescence* (TL) or *thermally stimulated luminescence* (TSL) analyzes the release of trapped carriers in a material when heated [24,25]. This release, often caused by defects acting as trap states, leads to luminescence that reveals the nature and characteristics of the defects.

While first-principles CTLs are thermodynamic quantities defined under equilibrium conditions, experimental probes often involve nonequilibrium processes (e.g., optical excitation or thermal activation). Nevertheless, CTLs serve as an essential reference point for interpreting and rationalizing experimental measurements of defect-related behavior in semiconductors and insulators.

Note: It is common in DFT studies to identify midgap defect levels by inspecting the density of states (DOS). However, this approach can be misleading. The electronic states obtained from Kohn-Sham DFT are only approximate and do not directly correspond to the true quasiparticle states that govern excitation energies. Apparent midgap peaks in the DFT DOS should not be assumed to represent true defect levels.

DFT is used primarily because it offers a good balance between computational efficiency and reasonable accuracy for a wide range of materials problems. However, its limitations must be recognized, especially when interpreting defect levels. For a more rigorous treatment of electronic excitations, many-body perturbation theory, such as the *GW* approximation [26], can be employed to calculate quasiparticle energies. Unfortunately, such methods are computationally demanding and often lack the ability to account for structural relaxation, particularly in the presence of defects. Because of these challenges, the most reliable way to determine defect levels within DFT is through the computation of charge transition levels (CTLs). CTLs provide a more physically meaningful estimate of the energetic position of defect-induced states relative to the band edges.

VI. WHAT ARE SHALLOW AND DEEP DEFECTS?

Charged defects must be ionized to release their associated electronic carriers (electrons or holes) for conduction.

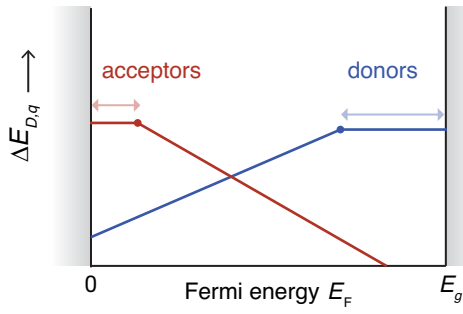


FIG. 5. The ionization energy of donor and acceptor defects.

The energy required for this ionization is critical: if the ionization energy is large, the carrier remains bound to the defect site and cannot contribute to conductivity. However, if the energy is small, typically within a few $k_B T$, thermal excitation can free the carrier into a conduction state, making it available as a free carrier. Here, k_B is the Boltzmann constant and T is the temperature.

The CTL position relative to the relevant band edge provides a direct measure of the ionization energy (Fig. 5). For donor-like defects, which donate electrons to the conduction band, the relevant quantity is the energy difference between the CTL and CBM. For acceptor-like defects, which accept electrons (equivalently, donate holes), the relevant comparison is with the VBM. The distance between the CTL and the corresponding band edge determines whether a defect is classified as shallow or deep:

- A defect is considered shallow if it has no CTL within the band gap (i.e., its stable charge state does not change over the Fermi energy range), implying that the defect level is resonant with the host bands. These defects are readily ionized and their carriers are effectively free.
- Another common case of shallow defects occurs when the CTL lies close to the band edge, typically within a few $k_B T$. In such cases, the bound carrier can be easily excited thermally into the conduction or valence band. For donor-like defects, this means that the CTL is near the CBM; and for acceptor-like defects, near the VBM. Figure 6 schematically illustrates these two scenarios for shallow donor defects: one with no CTL in the gap and one with a CTL close to the CBM.

In contrast, deep defects have CTLs located far from the band edges, generally more than a few $k_B T$ away (Fig. 7). The associated electronic carriers remain trapped at these deep levels and cannot participate in conduction. As a result, deep defects act as carrier traps, not contributors to free carrier concentrations. These defect states are sometimes referred to as midgap states.

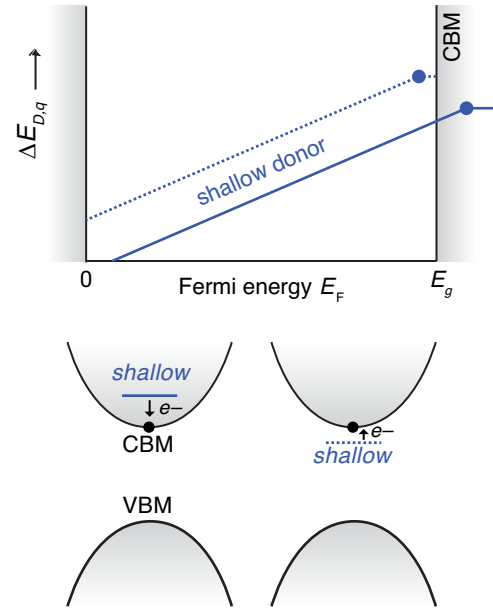
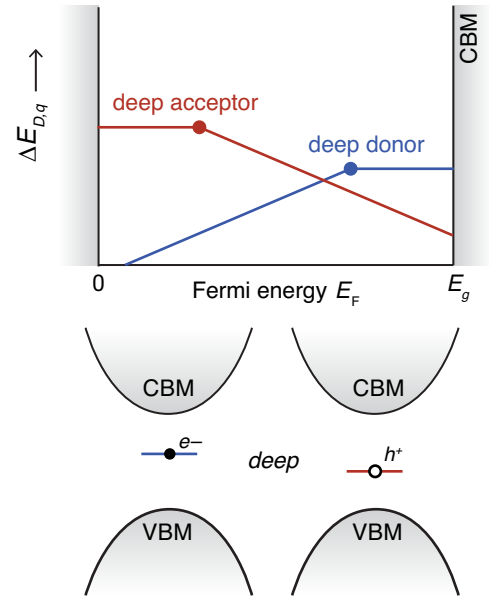


FIG. 6. Shallow donor defects feature defect states inside or close to the conduction band edge. Analogously, shallow acceptors feature defect states inside or close to the valence band edge.

Therefore, when analyzing a defect diagram, the presence of CTLs far from the band edges is a strong indicator of deep defects. However, it is important to keep in mind that the impact of such defects on material properties also

FIG. 7. Deep donors and acceptors introduce midgap states. Whether the states are occupied or unoccupied depends on the position of the Fermi energy (E_F). At 0 K, states below E_F are fully occupied and those above are fully unoccupied.

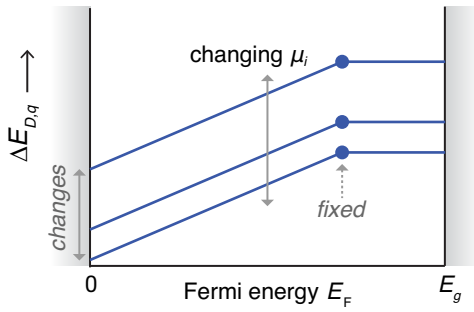


FIG. 8. The effect of changing elemental chemical potentials on the defect formation energy.

depends on their concentration, which leads us to the next important topic: the calculation of defect concentrations.

Note: In rare cases, an extremely deep donor defect will have CTLs that lie inside the valence band. Analogously, an extremely deep acceptor will have CTLs inside the conduction band.

VII. WHAT IS THE EFFECT OF ELEMENTAL CHEMICAL POTENTIALS?

The defect formation energy depends on the elemental chemical potentials of the constituent species (μ_i), as shown in Eq. (1). Consequently, defect diagrams are typically plotted for a fixed set of chemical potentials μ_i , where i denotes the elements present in the chemical phase space of the material. For instance, in ZnO, the defect formation energies depend on the chemical potentials of Zn and O; in a more complex material such as KGaSb₄, they depend on the chemical potentials of K, Ga, and Sb.

Mathematically, varying μ_i shifts the defect formation energies vertically in the defect diagram, which changes the y -axis intercept, while the slope (determined by the defect charge q) and the CTLs remain unchanged. This behavior is illustrated schematically in Fig. 8. In essence, changes in chemical potential modify the absolute formation energies of defects but do not alter their charge-state stability across the Fermi energy range.

The μ_i reflect the chemical environment during material growth or synthesis. Since the formation of a point defect involves the exchange of atoms between the material and external elemental reservoirs (grand canonical ensemble), the energy cost of this exchange is governed by the chemical potentials of the relevant elements. Thus, the synthesis conditions directly determine the values of μ_i . To illustrate this concept, consider ZnO grown under oxygen-rich (O-rich) versus oxygen-poor (O-poor) conditions [27]. Suppose that we are interested in the formation

of an oxygen vacancy, which involves removing an O atom from ZnO and placing it into the external O reservoir. Under O-rich conditions, the reservoir already contains a high concentration of oxygen, so inserting an additional O atom incurs a higher energetic penalty. In contrast, under O-poor conditions, where the oxygen chemical potential is lower, removing an O atom from ZnO and placing it into the reservoir is energetically more favorable. Therefore, the formation of oxygen vacancies is more favorable under O-poor conditions.

This example highlights how defect formation energies are strongly influenced by the thermodynamic conditions of synthesis. Careful control of the chemical environment allows for targeted defect engineering to optimize material properties [28,29].

VIII. HOW ARE DEFECT AND ELECTRONIC CARRIER CONCENTRATIONS CALCULATED?

The defect concentration at equilibrium is determined using statistical mechanics. The formation energy, along with the temperature and Fermi energy, is used in a Boltzmann distribution to calculate the equilibrium concentration of each defect:

$$[D_q] = N_s \times \exp\left(-\frac{\Delta E_{D,q}}{k_B T}\right), \quad (2)$$

where $[D_q]$ is the concentration of defect D in charge state q , N_s is the concentration of atomic sites at which D can form, k_B is the Boltzmann constant, and T is the temperature. The exponential term is essentially the probability of forming D , which when multiplied with the volumetric (or areal) site concentration, gives the volumetric (or areal) defect concentration. Typically, defect concentrations are expressed in numbers per unit volume (cm^{-3}).

Note: Equation (2) implicitly includes the configurational entropy contribution. However, it does not include the vibrational entropy contribution, which is generally negligible in most cases. The latter is an important consideration when defect formation involves elements that are gaseous under standard conditions. In such cases, the chemical potential of the elemental (gaseous) reservoir has strong T and pressure dependencies.

$\Delta E_{D,q}$ in Fig. 1(a) depends on E_F , but it is not clear at which E_F the defect concentration should be calculated. For this, we need to consider *charge neutrality*.

The defect and electronic carrier (electron, hole) concentrations are calculated by imposing the condition of

overall charge neutrality. This means that for the material to be charge neutral, the total number of positive and negative charges must be balanced. The positive charges include donor defects (positive slope in defect diagrams) and holes, and negative charges are acceptors (negative slope in defect diagrams) and electrons.

First, we need to choose a relevant temperature, typically, the synthesis or annealing temperature at which defects form and equilibrate. Next, we calculate the acceptor and donor defect concentrations as a function of E_F . Mathematically, $\Delta E_{D,q} = c + qE_F$, where c is the y -axis intercept in a defect diagram (Fig. 8). Neutral defects do not participate in charge balance. The electron and hole concentrations are given by the density of states $g(E)$ and the Fermi-Dirac distribution $f(E)$. Mathematically, $[e] = \int_{E_F}^{\infty} g(E)f_c(E)dE$ and $[h] = \int_{-\infty}^{E_F} g(E)f_v(E)dE$, where $f_c(E)$ and $f_v(E)$ are the Fermi-Dirac distribution functions for the conduction and valence bands, respectively. Here, $f_c(E)$ depends on E_F , E_{CBM} , and T and, similarly, $f_v(E)$ depends on E_F , E_{VBM} , and T . E_{CBM} and E_{VBM} are fixed quantities. The reader is referred to standard semiconductor textbooks for equations, including the simplified formula to calculate electron and hole concentrations in the nondegenerate limit using band effective masses instead of numerically performing the integrals discussed above.

Note how the only unknown in the equations to calculate defect and electron and hole concentrations is E_F ! We obtain the equilibrium Fermi energy, $E_{F,eq}$, by self-consistently solving the charge neutrality equation:

$$\sum_d (q_d [D]) + [h] = \sum_a (q_a [A]) + [e], \quad (3)$$

where a and d denote acceptor and donor defects, respectively. q_a and q_d are the corresponding charge states of the acceptor and donor defects, respectively. Terms in square brackets ($[]$) denote concentrations. The left-hand side of Eq. (3) is the total concentration of positive charges and the right-hand side is the negative charges. The charge neutrality equation is solved self-consistently (often, numerically) to obtain $E_{F,eq}$. Once $E_{F,eq}$ is determined, one can calculate the defect, individual electron and hole, and free net carrier concentrations.

There are several open-source PYTHON packages available for numerically solving $E_{F,eq}$. I recommend `py-scfermi`, developed by the groups of David Scanlon and Benjamin Morgan [30].

Note: This Tutorial focuses on the equilibrium thermodynamics of defect formation. While defects can—and often do—form under nonequilibrium conditions, determining their concentrations in such cases

is not straightforward and typically requires detailed experimental input. This is a specialized topic and falls outside the scope of this beginner-focused guide.

IX. HOW IS THE EQUILIBRIUM FERMI ENERGY ESTIMATED? WHAT INSIGHTS CAN BE GAINED?

While the exact position of the equilibrium Fermi energy ($E_{F,eq}$) must be determined by self-consistently solving the charge-neutrality condition [Eq. (3)], a useful first-order estimate can often be made by analyzing the defect diagram. To do this, one identifies the donor- and acceptor-type defects with the lowest formation energies. Since neutral defects do not contribute to charge balance, they are excluded from this consideration. $E_{F,eq}$ typically lies near the intersection point of the lowest-energy donor and acceptor defect lines [Fig. 1(a)]—this is the Fermi energy at which the formation energy of these oppositely charged defects are equal and their contributions to charge compensation are *approximately* balanced. This estimate not only provides a rough location of $E_{F,eq}$ but also offers qualitative insight into the dominant defect species and whether the material tends toward n -type or p -type behavior under given chemical conditions.

Note: This approach is an approximation and should be used with care. It can become unreliable when: (1) the band gap is small—because electron and hole concentrations are very sensitive to the location of $E_{F,eq}$ —and (2) the valence and conduction band effective masses differ significantly (e.g., by more than a factor of 5–10), which skews the density of states and alters the balance of electronic carriers. In such cases, the exact $E_{F,eq}$ must be determined by numerically solving the charge neutrality condition, which accounts for all charged defect and electronic carrier contributions.

X. CAN A MATERIAL BE DOPED n - or p -TYPE? WHAT DETERMINES DOPABILITY?

We learned earlier that donor-like defects tend to donate electrons, while acceptor-like defects accept electrons (or, equivalently, create holes). In most materials, both donor- and acceptor-like defects coexist. Whether a material is overall n -type or p -type depends on the relative concentrations of these charged defects. Intuitively, if donor defects (positively charged) are present in much higher concentrations than acceptors (negatively charged), the material will be n -type. This is because the excess positive charge from donors must be compensated, typically by the formation of free electrons. As a result, the equilibrium condition

leads to a higher electron concentration than hole concentration. This process is referred to as “self-doping” by native (intrinsic) defects.

In practical applications, materials are commonly doped with extrinsic dopants to control their electrical behavior—e.g., *n*-type Si doped with phosphorus or *n*-type ZnO doped with aluminum. However, not all materials can be extrinsically doped *n*- or *p*-type at will. The dopability is strongly influenced by the native defect chemistry of the material. Native defects such as Si vacancies in silicon or O vacancies in ZnO are inherently present and cannot be eliminated. Their formation energetics determine whether a material can generate additional free carriers from extrinsic doping.

In other words, whether a material is *n*-type, *p*-type, ambipolar, or insulating depends on its native defect chemistry. Figure 9 illustrates four representative scenarios: (1) *p*-type dopable, (2) *n*-type dopable, (3) both *p*- and *n*-type dopable (ambipolar), and (4) neither *n*- nor *p*-type (typical insulators). Understanding this interplay between native defects and extrinsic dopants is essential for designing materials with target electronic properties.

A. Scenario 1 (*p*-type dopable)

When native acceptor defects have low formation energies and native donor defects have relatively higher formation energies [as shown in Fig. 9(a)], the material tends to be *p*-type dopable. To illustrate this, consider a simplified case with one native acceptor (labeled *acceptor*) and one native donor (labeled *donor*). Now imagine introducing an extrinsic donor dopant [*d-dopant*, represented by a light dashed line with a positive slope in Fig. 9(a)]. $E_{F,eq}$ will be pinned near the intersection of the *acceptor* and *d-dopant* lines, closer to midgap than to the CBM. In this scenario, the material becomes lightly *n*-type or even remains *p*-type, depending on the formation energy of the native acceptor. This occurs because electrons introduced by the extrinsic donor dopant are largely compensated by holes generated from the native acceptor, the low formation energy of which ensures high concentration. Consequently, moderate to high electron concentrations cannot be achieved, limiting effective *n*-type doping. Now consider doping with an extrinsic acceptor dopant (*a-dopant*, represented by a dark dashed line with a negative slope). The Fermi level will now be near the intersection of the *donor* and *a-dopant* lines—typically near or even inside the valence band. This leads to strong *p*-type doping, with a high free hole concentration. Since the native donor has a high formation energy, the electron concentration remains low and the holes introduced by the extrinsic acceptor dopant are not significantly compensated. This qualitative analysis allows rapid assessment of dopability directly from a defect diagram. For quantitative predictions, however, one must compute $E_{F,eq}$ and carrier concentrations by

solving the charge-neutrality condition, as discussed in an earlier section. Notably, the qualitative conclusions drawn here will naturally emerge from such a more rigorous analysis.

We can define *p*-type and *n*-type dopability windows as metrics to assess the potential for extrinsic doping. These windows are defined based on the formation energies of native defects alone:

- The *p*-type dopability window is defined as the formation energy of the lowest-energy native donor defect evaluated at the VBM. This is illustrated by the double-headed arrow at the VBM in Fig. 9(a).
- Similarly, the *n*-type dopability window is the formation energy of the lowest-energy native acceptor defect at the CBM, shown at the CBM in Fig. 9(a).

These windows directly reflect the resistance of the material to compensating carriers introduced through doping:

- A large positive *p*-type dopability window indicates that native donors are difficult to form, making the material favorable for *p*-type doping.
- If the *p*-type dopability window is negative, native donors form easily and compensate holes, making *p*-type doping difficult.
- Conversely, a large positive *n*-type dopability window means that native acceptors are difficult to form at the CBM, allowing effective *n*-type doping.
- A negative *n*-type window suggests that native acceptors form readily, compensating electrons and hindering *n*-type doping.

In Fig. 9(a), the *p*-type dopability window is large and positive, while the *n*-type window is small and negative, indicating that the material is *p*-type dopable but resistant to *n*-type doping. $\text{Yb}_{14}\text{MnSb}_{11}$ is a well-known high-temperature-range thermoelectric material that is only *p*-type dopable (in fact, it is a degenerate *p*-type semiconductor even without extrinsic doping) due to the low formation energy of cation vacancies, which is a common feature of many Zintl thermoelectric materials.

Note: A material can natively be highly *p*-type or *n*-type doped due to the very low formation energy of native acceptors or donors, respectively, without being extrinsically doped.

B. Scenario 2 (*n*-type dopable)

The same analysis can be applied to Fig. 9(b), which illustrates an *n*-type dopable material. In this case, the low formation energy of the native donor defect makes *p*-type doping ineffective, as any holes introduced by extrinsic

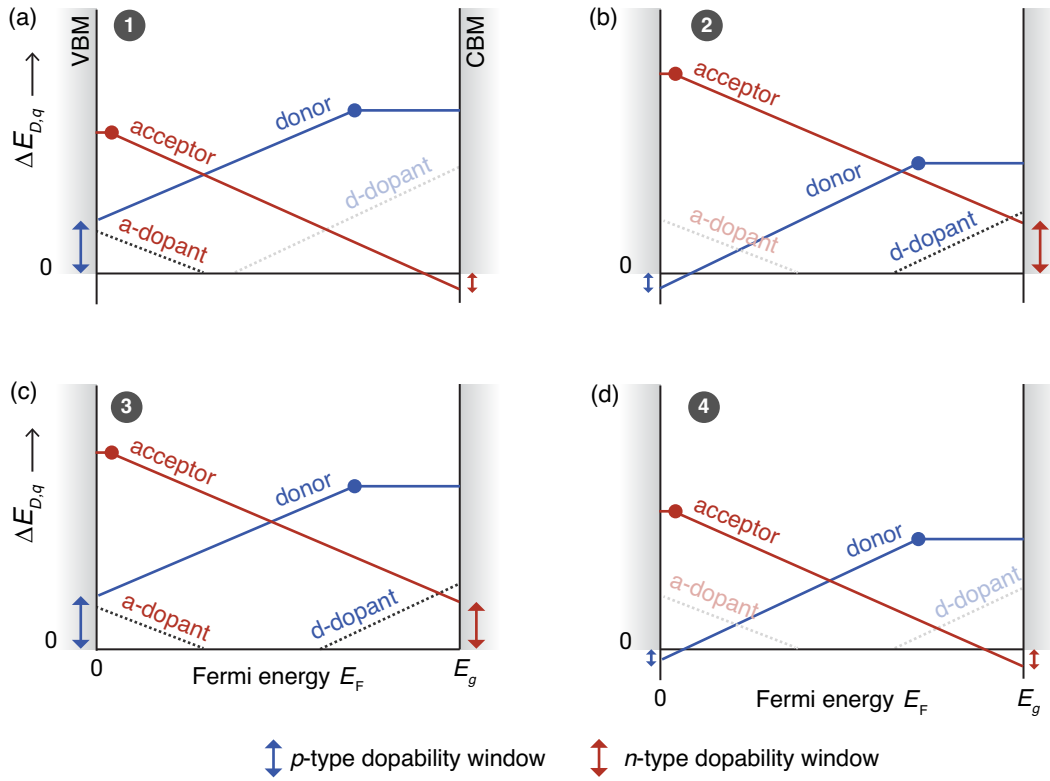


FIG. 9. Doping scenarios based on the native defect formation energies: 1, *p*-type dopable; 2, *n*-type dopable; 3, *n*- and *p*-type dopable; 4, not *n*- or *p*-type dopable. Defects labeled “donor” and “acceptor” are native defects, while “d-dopant” and “a-dopant” refer to extrinsic donor (*n*-type) and acceptor (*p*-type) extrinsic dopants, respectively.

acceptor dopants would be readily compensated. Conversely, the higher formation energy of the native acceptor allows for efficient extrinsic *n*-type doping. When the material is doped with an extrinsic donor dopant [represented as *d-dopant* in Fig. 9(b)], $E_{F,eq}$ shifts close to or inside the conduction band, resulting in a high free-electron concentration. This behavior is consistent with the negative *p*-type dopability window (due to the low formation energy of the native donor at the VBM) and the large positive *n*-type dopability window (due to the high formation energy of the native acceptor at the CBM), confirming the suitability for *n*-type doping. ZnO is a well-known material that is readily *n*-type dopable but in which high levels of *p*-type doping cannot be achieved.

C. Scenario 3 (*n*- and *p*-type dopable)

A material can also be dopable both *n*-type and *p*-type, which is referred to as ambipolar dopable, as illustrated in Fig. 9(c). This situation arises when the native donor and acceptor defects both have relatively high formation energies, resulting in large positive *n*- and *p*-type dopability windows. In such cases, extrinsic dopants—donors or acceptors—can efficiently generate free electrons or holes, respectively, without significant compensation by native defects. A classic example is silicon, which can

be doped *p*-type with boron and *n*-type with phosphorus or arsenic. This ambipolar dopability is a cornerstone of modern microelectronics. Ambipolar materials are highly desirable in energy and optoelectronic applications due to their flexibility in device design, ease of fabrication, and compatibility with a wide range of processing conditions.

D. Scenario 4 (not *n*- or *p*-type dopable)

By this point, the reader should have developed a solid understanding of how to interpret defect diagrams for assessing dopability. Figure 9(d) illustrates a case in which the material is neither *n*-type nor *p*-type dopable, resulting in an insulator with intrinsically low free carrier concentrations. As an exercise, the reader is encouraged to analyze the defect diagram in Fig. 9(d) and verify that the material lacks favorable conditions for effective doping in either direction. This will help reinforce the concepts of dopability windows and the role of native defect energetics in determining the electrical behavior of a material.

Note: A material may exhibit potential for doping in a specific manner, such as *p*-type, *n*-type, or ambipolar (scenarios 1–3), but whether it is actually doped depends on identifying a suitable dopant that is both

shallow (i.e., low ionization energy) and highly soluble in the host material. In other words, dopability reflects the possibility of successful doping, not a guarantee of it.

XI. PRACTICAL EXAMPLES FROM ENERGY RESEARCH

Several practical examples from energy research where defect calculations are critical for material design and for gaining mechanistic insights are now discussed. Each case illustrates how understanding and tuning defects can help achieve better performance in energy applications. *The examples presented in this section are intended for illustrative purposes only.* For the most up-to-date understanding of defect physics in the specific materials discussed, readers are encouraged to consult the current literature and apply the concepts introduced in this Tutorial. Note that I do not focus here on the computational details such as the level of DFT theory used, band-gap corrections, or other methodological specifics. Instead, our emphasis is solely on interpreting defect formation energy and energy level diagrams.

Note: The choice of exchange-correlation functional in DFT plays a critical role in defect calculations, as it strongly influences both the localization of electronic states and the position of band edges. These factors, in turn, *qualitatively* and *quantitatively* affect key defect properties such as formation energies, charge-transition levels, and carrier concentrations. For instance, generalized gradient approximation (GGA) functionals often underestimate band gaps and delocalize defect states, while hybrid functionals such as HSE06 or many-body *GW* offer improved accuracy [8,31,32].

A. Photovoltaics—Defects in halide perovskites

Defects in lead halide perovskites such as (MA)PbI₃ (MA = methylammonium) strongly influence non-radiative recombination, carrier lifetimes, and device stability. Remarkably, these materials tolerate relatively high defect densities while maintaining good performance, which is often attributed to the dominance of shallow defects and absence of deep defects—an assertion that has been intensely debated because of contradictory experimental and computational findings.

Figure 10 reproduces the calculated defect formation energy (DFE) in MAPbI₃, as reported in Ref. [33]. The defect diagram corresponds to moderately iodine-rich (“I-med”) growth conditions and plots the formation energy as a function of E_F across a band gap of 1.6 eV.

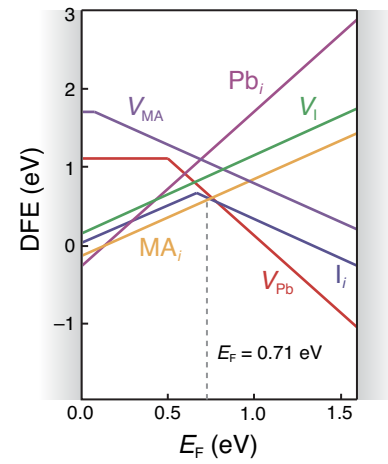


FIG. 10. A plot of the defect formation energy (DFE) versus the Fermi energy (E_F) for MAPbI₃, showing the most stable defects in iodine-medium (I-med, stoichiometric) growth conditions. E_F ranges from the valence band maximum (VBM) to the CBM. Redrawn from Ref. [33].

At the calculated equilibrium Fermi energy ($E_{F,eq} = 0.71$ eV above the valence band maximum), the dominant defects, i.e., those with the lowest formation energies, are the lead vacancy (V_{Pb}), the iodine interstitial (I_i), and the methylammonium interstitial (MA_i). In contrast, the iodine vacancy (V_I), lead interstitial (Pb_i), and methylammonium vacancy (V_{MA}) exhibit higher formation energies and are thus expected to occur in lower concentrations under I-med conditions. Notably, $E_{F,eq}$ lies near the intersection of the lowest-energy acceptor (I_i^{-1}) and donor (MA_i^{+1}) defects. Among these, MA_i , V_I , Pb_i , and V_{MA} (with charge-transition level <0.1 eV above the VBM) are shallow defects, while I_i and V_{Pb} introduce deep midgap states. This defect diagram reveals two key insights:

- (1) Not all defects with low formation energies in MAPbI₃ are shallow—both I_i and V_{Pb} are high-concentration deep defects.
- (2) The low formation energies of I_i and MA_i suggest significant ionic mobility, which has been associated with performance degradation and hysteresis in MAPbI₃-based solar cells.

B. Thermoelectrics—Dopability of Mg₃Sb₂

The conversion efficiency of thermoelectric materials is highly sensitive to carrier concentration, which is often controlled through native (intrinsic) defects and extrinsic doping. Defects can also influence lattice thermal conductivity by acting as phonon scattering centers. Defect

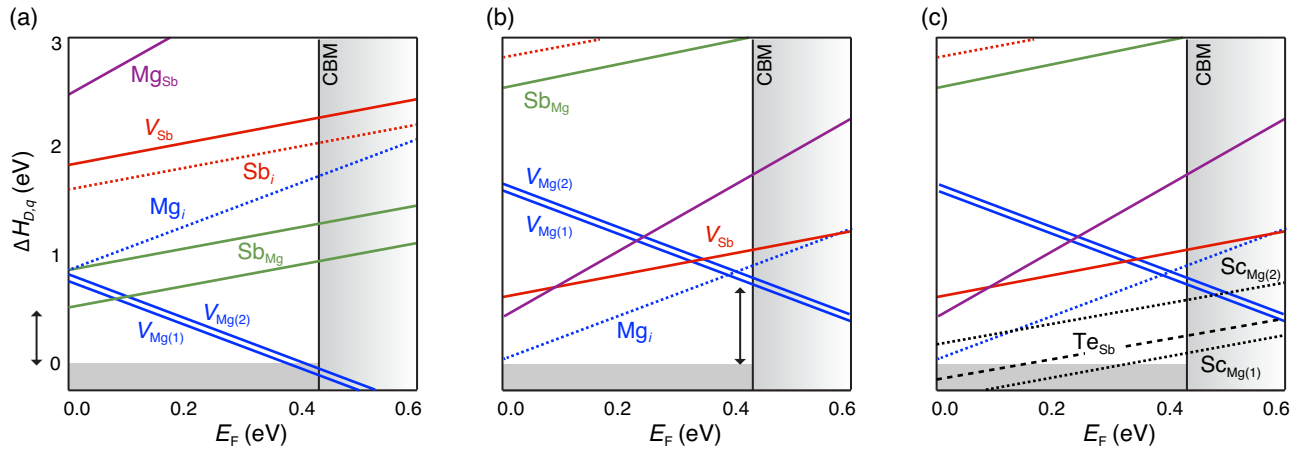


FIG. 11. The formation energetics of native defects in Mg_3Sb_2 under (a) Mg-poor and (b) Mg-rich growth conditions. Subscripts (1) and (2) denote the unique Mg Wyckoff sites. E_F ranges from 0 eV (VBM) to 0.45 eV (CBM). The double-headed arrows denote the dopability windows for (a) p -type and (b) n -type. (c) The formation energies of substitutional n -type dopants Te and Sc on the Sb and Mg site, respectively. Redrawn from Ref. [34].

diagrams are used to predict dopability and identify majority charge carriers. They also aid in identifying suitable dopants to achieve desired n - or p -type conductivity.

The calculated formation energies of native defects in Mg_3Sb_2 , a high-performance thermoelectric material, are shown in Fig. 11 under Mg-poor and Mg-rich growth conditions. These calculations highlight the ambipolar doping behavior of the material. Under Mg-poor conditions [Fig. 11(a)], the low formation energy of the acceptor-like Mg vacancy (V_{Mg}) leads to intrinsic p -type conductivity. Moreover, the large p -type dopability window under these conditions allows further enhancement of the free-hole concentration via extrinsic p -type doping. Historically, Mg_3Sb_2 was believed to be only p -type dopable because typical synthesis conditions were Mg-poor, largely due to the high volatility of Mg. However, as shown in Fig. 11(b), defect calculations have revealed a dramatic shift in dopability under Mg-rich growth conditions. Here, the formation energy of V_{Mg} increases significantly, effectively closing the p -type window while opening a large n -type dopability window. Under these conditions, the Mg interstitial (Mg_i), a donor defect, has a low formation energy, and dominates the defect chemistry, resulting in n -type conductivity. This shift in understanding has been pivotal: the ability to dope Mg_3Sb_2 n -type has unlocked its exceptional thermoelectric performance and attracted significant interest from the research community. In thermoelectrics, tuning the majority carrier concentration (electrons in the n -type case) is critical for optimizing device performance. Defect calculations have also guided the successful identification of suitable extrinsic n -type dopants such as Te and group-3 elements (Sc, Y, and La), which can achieve high free-electron concentrations on the order of approximately 10^{20} – 10^{21} cm^{-3} [Fig. 11(c)]. In summary, defect calculations teach us that:

- (1) Mg_3Sb_2 is ambipolar but achieving either p -type or n -type conductivity requires appropriate control of the growth conditions.
- (2) The large n -type dopability window under Mg-rich conditions enables effective extrinsic n -type doping, with dopants such as Te and group-3 elements achieving high free-electron concentrations.

C. Solid-state batteries—Diffusion mechanism and aliovalent doping of Na_3Sb_4

Solid-state ion diffusion is mediated by native point defects, e.g., Na vacancies in Na_3Sb_4 . The ionic conductivity (σ_{ion}) of solid electrolytes (SEs) directly depend on the mobile ion defect concentration (n). Mathematically, $\sigma_{\text{ion}} = n\mu qe$, where μ is the ion mobility, q is the ion charge, and e is the fundamental electronic charge (a constant). Defect diagrams help us identify the dominant mobile ion defect (vacancy versus interstitial) that determines the primary diffusion mechanism. Aliovalent doping, in which a dopant of a differing charge from the host lattice is intentionally introduced, is one approach to enhancing σ_{ion} . The charge imbalance is compensated by creating more charged mobile ion defects (n increases) in the SE. This approach has been demonstrated for several SEs. While aliovalent doping is effective, dopant selection has been mainly driven by chemical intuition and trial and error. Defect calculations offer a fast and effective route to identification of suitable aliovalent dopants.

Let us consider Na_3Sb_4 , a well-known Na-ion solid electrolyte that exhibits some of the highest reported ionic conductivities. The calculated defect diagram for Na_3Sb_4 is shown in Fig. 12 (only the lowest formation energy defects are labeled for clarity). Na vacancies (V_{Na}) have significantly lower formation energies than Na interstitials (Na_i), leading to equilibrium concentrations of V_{Na} that are

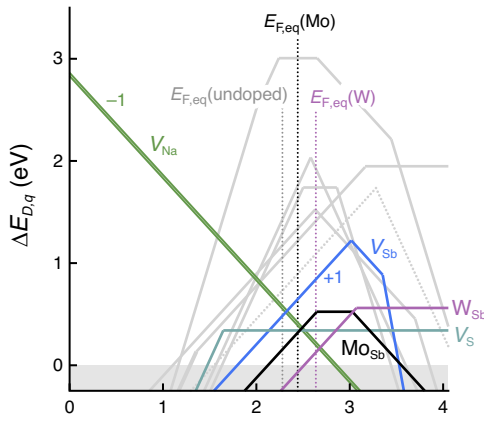


FIG. 12. The formation energy ($\Delta E_{D,q}$) of relevant native defects and substitutional dopants (W, Mo) in Na_3Sb_4 . The equilibrium Fermi energy ($E_{F,\text{eq}}$) is calculated at 823 K. Aliovalent doping moves $E_{F,\text{eq}}$ toward the CBM, lowering $\Delta E_{D,q}$ of V_{Na} . Redrawn from Ref. [35].

roughly 3 orders of magnitude higher than those of Na_i . This supports the widely accepted mechanism that Na^+ diffusion in Na_3Sb_4 is mediated by V_{Na} .

Figure 12 also includes the calculated formation energies of aliovalent substitutional dopants, W_{Sb} and Mo_{Sb} , where W and Mo substitute Sb. These donor dopants exhibit low formation energies, indicating that they can be readily incorporated. Importantly, W and Mo doping shifts the equilibrium Fermi energy ($E_{F,\text{eq}}$) toward the CBM, which in turn lowers the formation energy of V_{Na} . This leads to an increased concentration of mobile V_{Na} , which has been experimentally shown to enhance the ionic conductivity of Na_3Sb_4 by factors of approximately 30 (for W) and approximately 3 (for Mo). As a thought experiment, consider the alternative scenario in which Na-ion diffusion in Na_3Sb_4 is mediated by Na interstitials instead. Since interstitial Na is positively charged (a donor), increasing its concentration would require p -type (acceptor) aliovalent doping, which would shift the Fermi energy toward the valence band and lower the formation energy of Na_i . From this defect diagram, we learn two key insights:

- Na vacancies are the dominant Na-ion defects responsible for ionic conduction in Na_3Sb_4 .
- Aliovalent donor doping (e.g., with W or Mo) is an effective strategy for enhancing σ_{ion} by increasing V_{Na} concentrations through Fermi-level tuning.

D. Power electronics—Dopability and doping of $\beta\text{-Ga}_2\text{O}_3$

$\beta\text{-Ga}_2\text{O}_3$ (monoclinic) is a wide bandgap semiconductor that has garnered significant interest in power electronics due to its large breakdown field (approximately 8 MV/cm), high Baliga figure of merit, and potential for

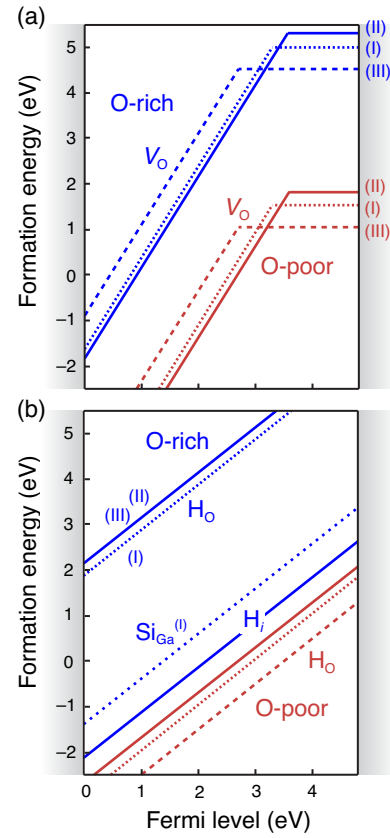


FIG. 13. (a) The formation energy in $\beta\text{-Ga}_2\text{O}_3$ versus the Fermi level for the oxygen vacancy (V_{O}) under O-rich and O-poor conditions. The labels (I), (II), and (III) refer to the three inequivalent O Wyckoff sites. (b) The formation energy versus the Fermi level for H-related defects, including H_{O} and H_{i} as well as substitutional $\text{Si}_{\text{Ga}}^{(\text{I})}$ on Ga site (I) under O-rich conditions. Redrawn from Ref. [36].

high-efficiency devices. However, the practical realization of $\beta\text{-Ga}_2\text{O}_3$ -based devices depends critically on defect physics, especially the native defects and extrinsic doping strategies. Defect calculations have shown that oxygen vacancies (V_{O}), often assumed to be the source of the observed n -type conductivity, are deep donors [Fig. 13(a)] and, therefore, cannot contribute free electrons. Instead, the n -type conductivity is attributed to common background impurities such as silicon and hydrogen, as evidenced by the low formation energy of shallow Si_{Ga} and H_{i} defects [Fig. 13(b)]. $\beta\text{-Ga}_2\text{O}_3$ is notoriously hard to dope p -type, which again is evident from the defect diagram in Fig. 13(a), where the low formation energy of native donor defects, mainly V_{O} , even under O-rich conditions, prevents the opening of a p -type dopability window. We learn the following about $\beta\text{-Ga}_2\text{O}_3$:

- The V_{O} are deep donor defects and, therefore, cannot be responsible for observed n -type conductivity.

- (2) Low formation energy native donor defects such as V_O limit p -type doping, at least under equilibrium conditions.

XII. CONCLUDING REMARKS

The central role of defects in enabling both functional and structural properties of materials is often underappreciated. This Tutorial has been inspired by my frequent interactions with experimentalists and fellow computational researchers who have sought clarity on how to interpret defect formation energy and energy-level diagrams. It also stems from my experience as a peer reviewer, where I have repeatedly encountered common pitfalls, both misinterpretation and overinterpretation, of defect diagrams, often leading to incorrect conclusions. Looking back, I wish I had access to a systematic resource such as this when I first started working on defects. While the interpretation of defect diagrams is critical, it is equally important to acknowledge that the calculations themselves involve many moving parts. Even if the diagrams are correctly read, methodological choices such as the level of theory, treatment of finite-size effects, or band edge corrections can lead to significant inaccuracies if not carefully addressed.

The good news is that the field has come a long way. Compared to a decade ago, there are now more computational tools, methodological advances, and community resources (pylada-defects [13], pyCDT [16], pymatgen-analysis-defects [37], doped [38]) that make defect calculations more accessible, reproducible, and robust. Open-source tools for plotting defect diagrams, such as pyCDT [16] and VTAnDeM [39], have also been developed. Defect modeling has become more mainstream, yet misinterpretation remains common, which highlights the need for foundational practical guidance such as this Tutorial. While this Tutorial has focused on point defects in crystalline semiconductors under equilibrium and dilute conditions, I would be remiss not to mention important frontiers such as extended defects, nonequilibrium populations, high defect concentrations, and defect physics in disordered materials. In materials in which defects strongly localize charge, such as in polaron-forming materials, standard defect level diagrams may be insufficient, and additional considerations related to charge localization and lattice relaxation are needed to accurately capture defect behavior [40–42]. While defect formation energies are often treated as temperature independent, temperature can influence defect thermodynamics through mainly entropy contributions. Beyond configurational entropy, vibrational, electronic, and magnetic entropy can all lead to temperature-dependent defect formation energies and charge-transition levels [43–45]. Additionally, temperature affects the chemical potentials of constituent elements and the band gap, both of which can significantly alter

predicted carrier concentrations, especially when comparing to experimental measurements at elevated temperatures [46].

These are exciting areas that offer rich opportunities for methodological development and new physical insights. I hope this Tutorial has helped to demystify the language and visual conventions of defect calculations, lower the barrier for new entrants to the field, and promote more accurate interpretation of these powerful tools.

ACKNOWLEDGMENTS

I am grateful to Vladan Stevanović, for his mentorship and for fostering a rigorous understanding of defect physics. I also thank Stephan Lany and Anuj Goyal for numerous insightful discussions during that time, which shaped my approach to interpreting and presenting defect and defect level diagrams. My appreciation extends to my experimental collaborators at the Colorado School of Mines, the National Renewable Energy Laboratory, and Northwestern University, whose perspectives and questions greatly influenced how I communicate these concepts across disciplinary boundaries. Finally, I acknowledge the contributions of David Scanlon, Aron Walsh, and Chris Van de Walle, who are not direct collaborators, but their pioneering work in first-principles defect calculations has been a continual source of inspiration.

DATA AVAILABILITY

No data were created or analyzed in this study.

-
- [1] A. Walsh and A. Zunger, Instilling defect tolerance in new compounds, *Nat. Mater.* **16**, 964 (2017).
 - [2] J. S. Park, S. Kim, Z. Xie, and A. Walsh, Point defect engineering in thin-film solar cells, *Nat. Rev. Mater.* **3**, 194 (2018).
 - [3] S. Nakamura, T. Mukai, and M. Senoh, Candela-class high-brightness InGaN/AlGaIn double-heterostructure blue-light-emitting diodes, *Appl. Phys. Lett.* **64**, 1687 (1994).
 - [4] H. L. Tuller, Defect engineering: Design tools for solid state electrochemical devices, *Electrochim. Acta* **48**, 2879 (2003).
 - [5] P. Gorai, T. Famprakis, B. Singh, V. Stevanović, and P. Canepa, Devil is in the defects: Electronic conductivity in solid electrolytes, *Chem. Mater.* **33**, 7484 (2021).
 - [6] Y. Murakami, Material defects as the basis of fatigue design, *Int. J. Fatigue* **41**, 2 (2012).
 - [7] S. Lany and A. Zunger, Assessment of correction methods for the band-gap problem and for finite-size effects in supercell defect calculations: Case studies for ZnO and GaAs, *Phys. Rev. B* **78**, 235104 (2008).
 - [8] H. Peng, D. O. Scanlon, V. Stevanovic, J. Vidal, G. W. Watson, and S. Lany, Convergence of density and hybrid functional defect calculations for compound semiconductors, *Phys. Rev. B* **88**, 115201 (2013).

- [9] C. Freysoldt, B. Grabowski, T. Hickel, J. Neugebauer, G. Kresse, A. Janotti, and C. G. Van de Walle, First-principles calculations for point defects in solids, *Rev. Mod. Phys.* **86**, 253 (2014).
- [10] H.-P. Komsa, T. T. Rantala, and A. Pasquarello, Finite-size supercell correction schemes for charged defect calculations, *Phys. Rev. B* **86**, 045112 (2012).
- [11] Y. Kumagai and F. Oba, Electrostatics-based finite-size corrections for first-principles point defect calculations, *Phys. Rev. B* **89**, 195205 (2014).
- [12] S. Kim, S. N. Hood, J.-S. Park, L. D. Whalley, and A. Walsh, Quick-start guide for first-principles modelling of point defects in crystalline materials, *J. Phys.: Energy* **2**, 036001 (2020).
- [13] A. Goyal, P. Gorai, H. Peng, S. Lany, and V. Stevanović, A computational framework for automation of point defect calculations, *Comput. Mater. Sci.* **130**, 1 (2017).
- [14] M. H. Naik and M. Jain, CoFFEE: Corrections for formation energy and eigenvalues for charged defect simulations, *Comput. Phys. Commun.* **226**, 114 (2018).
- [15] E. Péan, J. Vidal, S. Jobic, and C. Latouche, Presentation of the PyDEF post-treatment PYTHON software to compute publishable charts for defect energy formation, *Chem. Phys. Lett.* **671**, 124 (2017).
- [16] D. Broberg, B. Medasani, N. E. R. Zimmermann, G. Yu, A. Canning, M. Haranczyk, M. Asta, and G. Hautier, PyCDT: A PYTHON toolkit for modeling point defects in semiconductors and insulators, *Comput. Phys. Commun.* **226**, 165 (2018).
- [17] N. M. Johnson, D. J. Bartelink, R. B. Gold, and J. F. Gibbons, Constant-capacitance DLTS measurement of defect-density profiles in semiconductors, *J. Appl. Phys.* **50**, 4828 (1979).
- [18] M. Zhou, W. Wang, J. Lu, and Z. Ni, How defects influence the photoluminescence of TMDCs, *Nano Res.* **14**, 29 (2021).
- [19] R. Sauer and J. Weber, Photoluminescence characterization of deep defects in silicon, *Physica B+C* **116**, 195 (1983).
- [20] H. Nan, Z. Wang, W. Wang, Z. Liang, Y. Lu, Q. Chen, D. He, P. Tan, F. Miao, X. Wang, *et al.*, Strong photoluminescence enhancement of MoS₂ through defect engineering and oxygen bonding, *ACS Nano* **8**, 5738 (2014).
- [21] G. D. Watkins and J. W. Corbett, Defects in irradiated silicon: Electron paramagnetic resonance of the divacancy, *Phys. Rev.* **138**, A543 (1965).
- [22] L. S. Vlasenko and G. D. Watkins, Optical detection of electron paramagnetic resonance for intrinsic defects produced in ZnO by 2.5-MeV electron irradiation *in situ* at 4.2 K, *Phys. Rev. B* **72**, 035203 (2005).
- [23] M. Fanciulli and T. D. Moustakas, Study of defects in wide band gap semiconductors by electron paramagnetic resonance, *Phys. B: Condens. Matter* **185**, 228 (1993).
- [24] S. W. S. McKeever, *Thermoluminescence of Solids* (Cambridge University Press, 1985), Vol. 3.
- [25] E. T. Rodine and P. L. Land, Electronic defect structure of single-crystal ThO₂ by thermoluminescence, *Phys. Rev. B* **4**, 2701 (1971).
- [26] F. Aryasetiawan and O. Gunnarsson, The *GW* method, *Rep. Prog. Phys.* **61**, 237 (1998).
- [27] A. F. Kohan, G. Ceder, D. Morgan, and C. G. Van de Walle, First-principles study of native point defects in ZnO, *Phys. Rev. B* **61**, 15019 (2000).
- [28] P. Gorai, D. Krasikov, S. Grover, G. Xiong, W. K. Metzger, and V. Stevanović, A search for new back contacts for CdTe solar cells, *Sci. Adv.* **9**, eade3761 (2023).
- [29] M. Y. Toriyama, J. Qu, G. Jeffrey Snyder, and P. Gorai, Defect chemistry and doping of BiCuSeO, *J. Mater. Chem. A* **9**, 20685 (2021).
- [30] A. G. Squires, D. O. Scanlon, and B. J. Morgan, PY-SC-FERMI: Self-consistent Fermi energies and defect concentrations from electronic structure calculations, *J. Open Source Software* **8** (2023).
- [31] A. Alkauskas, P. Broqvist, and A. Pasquarello, Defect energy levels in density functional calculations: Alignment and band gap problem, *Phys. Rev. Lett.* **101**, 046405 (2008).
- [32] W. Chen and A. Pasquarello, Accuracy of *GW* for calculating defect energy levels in solids, *Phys. Rev. B* **96**, 020101 (2017).
- [33] D. Meggiolaro, S. G. Motti, E. Mosconi, A. J. Barker, J. Ball, C. A. R. Perini, F. Deschler, A. Petrozza, and F. De Angelis, Iodine chemistry determines the defect tolerance of lead-halide perovskites, *Energy & Environ. Sci.* **11**, 702 (2018).
- [34] P. Gorai, E. S. Toberer, and V. Stevanović, Effective *n*-type doping of Mg₃Sb₂ with group-3 elements, *J. Appl. Phys.* **125**, 025105 (2019).
- [35] C.-W. Lee, M. Maegawa, H. Akamatsu, K. Hayashi, S. Ohno, and P. Gorai, Local and global structural effects of doping on ionic conductivity in the Na₃SbS₄ solid electrolyte, *ACS Mater. Lett.* **7**, 620 (2025).
- [36] J. B. Varley, J. R. Weber, A. Janotti, and C. G. Van de Walle, Oxygen vacancies and donor impurities in β -Ga₂O₃, *Appl. Phys. Lett.* **97**, 142106 (2010).
- [37] J.-X. Shen and J. Varley, PYMATGEN-ANALYSIS-DEFECTS: A PYTHON package for analyzing point defects in crystalline materials, *J. Open Source Software* **9**, 5941 (2024).
- [38] S. R. Kavanagh, A. G. Squires, A. Nicolson, I. Mosquera-Lois, A. M. Ganose, B. Zhu, K. Brlec, A. Walsh, and D. O. Scanlon, DOPED: PYTHON toolkit for robust and repeatable charged defect supercell calculations, *J. Open Source Software* **9** (2024).
- [39] M. Y. Toriyama, J. Qu, L. C. Gomes, and E. Ertekin, VTAn-DeM: A PYTHON toolkit for simultaneously visualizing phase stability, defect energetics, and carrier concentrations of materials, *Comput. Phys. Commun.* **287**, 108691 (2023).
- [40] S. Falletta and A. Pasquarello, Polarons free from many-body self-interaction in density functional theory, *Phys. Rev. B* **106**, 125119 (2022).
- [41] C. Franchini, M. Reticcioli, M. Setvin, and U. Diebold, Polarons in materials, *Nat. Rev. Mater.* **6**, 560 (2021).
- [42] W. Hong Sio, C. Verdi, S. Poncé, and F. Giustino, *Ab initio* theory of polarons: Formalism and applications, *Phys. Rev. B* **99**, 235139 (2019).
- [43] S. Qiao, Y.-N. Wu, X. Yan, B. Monserrat, S.-H. Wei, and B. Huang, Temperature effect on charge-state transition levels of defects in semiconductors, *Phys. Rev. B* **105**, 115201 (2022).

- [44] I. Mosquera-Lois, J. Klarbring, and A. Walsh, Point defect formation at finite temperatures with machine learning force fields, *Chem. Sci.* **16**, 8878 (2025).
- [45] B. Grabowski, T. Hickel, and J. Neugebauer, Formation energies of point defects at finite temperatures, *Phys. Status Solidi (b)* **248**, 1295 (2011).
- [46] K. Aaditta Arnab, M. Stephens, I. Maxfield, C. Lee, E. Ertekin, Y. K. Frodason, J. B. Varley, and M. A. Scarpulla, Quantitative modeling of point defects in β -Ga₂O₃ combining hybrid functional energetics with semiconductor and processes thermodynamics, *Phys. Chem. Chem. Phys.* **27**, 11129 (2025).